Inland thinning on the Greenland ice sheet controlled by outlet glacier geometry

Denis Felikson[1,2]*, Timothy C. Bartholomaus[1†], Ginny A. Catania[1,3], Niels J. Korsgaard[4], Kurt H. Kjær[5], Mathieu Morlighem[6], Brice Noël[7], Michiel van den Broeke[7], Leigh A. Stearns[8], Emily L. Shroyer[9], David A. Sutherland[10] and Jonathan D. Nash[9]

Greenland's contribution to future sea-level rise remains uncertain and a wide range of upper and lower bounds has been proposed. These predictions depend strongly on how mass loss—which is focused at the termini of marine-terminating outlet glaciers—can penetrate inland to the ice-sheet interior. Previous studies have shown that, at regional scales, Greenland ice sheet mass loss is correlated with atmospheric and oceanic warming. However, mass loss within individual outlet glacier catchments exhibits unexplained heterogeneity, hindering our ability to project ice-sheet response to future environmental forcing. Using digital elevation model differencing, we spatially resolve the dynamic portion of surface elevation change from 1985 to present within 16 outlet glacier catchments in West Greenland, where significant heterogeneity in ice loss exists. We show that the up-glacier extent of thinning and, thus, mass loss, is limited by glacier geometry. We find that 94% of the total dynamic loss occurs between the terminus and the location where the down-glacier advective speed of a kinematic wave of thinning is at least three times larger than its diffusive speed. This empirical threshold enables the identification of glaciers that are not currently thinning but are most susceptible to future thinning in the coming decades.

Mass loss from the Greenland ice sheet (GrIS) has accelerated since 2005 and is concentrated near the southeast and northwest margins[1–4]. Numerous studies have described spatiotemporal heterogeneity in outlet glacier terminus retreat[5], surface elevation[6], and velocity change[7] that influence where and when mass is lost from the ice sheet. At the ~500 km scale, average changes correlate with atmospheric and oceanic temperature increases[8–11]. However, individual glaciers contribute to ice sheet mass loss disproportionately from their catchment area[12] and no mechanism exists to explain the observed heterogeneity of mass loss within individual glacier catchments. Previous work has shown that glacier retreat is initiated as a perturbation to the force balance at the terminus, causing thinning that propagates up-glacier[13,14] at different rates[15]. Inland thinning can account for more than 75% of total mass loss from a glacier catchment[13] and uncertainty in the extent of inland thinning strongly influences Greenland's contribution to future sea-level rise, for which a wide range of upper and lower bounds is given in the literature (46 mm–538 mm by year 2100; refs 13,16–18).

Spatial heterogeneity of observed mass change

To fully resolve the complex pattern of outlet glacier behaviour, we calculate mass change from surface elevation changes in West Greenland using high-resolution digital elevation models (DEMs) from a 1985 aerial survey of the region[19] and WorldView stereo imagery collected from 2012 to 2015 (Supplementary Table 1). These data sets provide unprecedented spatial resolution (25 m) of surface elevation change. By differencing the DEMs and removing the component of mass change due to surface mass balance (Methods, Supplementary Fig. 1), we obtain estimates of dynamic mass loss in the near-terminus regions of outlet glaciers (Fig. 1), revealing significant spatial variability in dynamic mass loss among glaciers (−0.1 Gt to −190 Gt; Supplementary Table 2). The high spatial resolution of the DEMs and a new model-derived estimate of bed topography[20] allow us to resolve the upstream limits of dynamic thinning within glacier catchments and explain, through kinematic wave theory[21], why the inland extent of dynamic thinning varies from glacier to glacier, thus providing an explanation for the heterogeneity in observed mass loss.

We find that, of the 16 glacier catchments in West Greenland, four have dynamically gained mass since 1985 and their termini have remained stable: Rink Isbræ (RNK), Kangerlussuup Sermersua (KAS), Store Gletsjer (STR) and Sermeq Avannarleq (AVA) (Supplementary Table 2). The remaining 12 catchments have dynamically lost mass, although the amount and spatial extent of this dynamic thinning varies (Fig. 1). Hereafter, we refer to dynamic thinning and dynamic mass loss simply as thinning and mass loss, respectively. In the Sermeq Kujalleq (KUJ) catchment, thinning extends 15 km up-glacier from its terminus, whereas the Jakobshavn Isbræ (JAK) catchment has thinned to 120 km up-glacier from its present-day terminus[22]. Consistent with past studies[9,11], but at higher spatial resolution, we find that retreat and thinning are linked; glaciers that have undergone the largest retreats have also experienced the greatest thinning (Umiammakku Isbræ (UMI), Sermeq Silarleq (SIL),

[1]Institute for Geophysics, University of Texas at Austin, Austin, Texas 78758, USA. [2]Department of Aerospace Engineering and Engineering Mechanics, University of Texas at Austin, Austin, Texas 78705, USA. [3]Department of Geological Sciences, University of Texas at Austin, Austin, Texas 78705, USA. [4]Nordic Volcanological Center, Institute of Earth Sciences, University of Iceland, IS-101 Reykjavik, Iceland. [5]Centre for GeoGenetics, Natural History Museum, University of Copenhagen, Copenhagen 1350, Denmark. [6]Department of Earth System Science, University of California, Irvine, California 92697, USA. [7]Institute for Marine and Atmospheric Research Utrecht, Utrecht University, 3584 CC Utrecht, The Netherlands. [8]Department of Geology, University of Kansas, Lawrence, Kansas 66045, USA. [9]College of Earth, Ocean, and Atmospheric Sciences, Oregon State University, Corvallis, Oregon 97331, USA. [10]Department of Geological Sciences, University of Oregon, Eugene, Oregon 97403, USA. †Present address: Department of Geological Sciences, University of Idaho, Moscow, Idaho 83844, USA. *e-mail: denis.felikson@utexas.edu
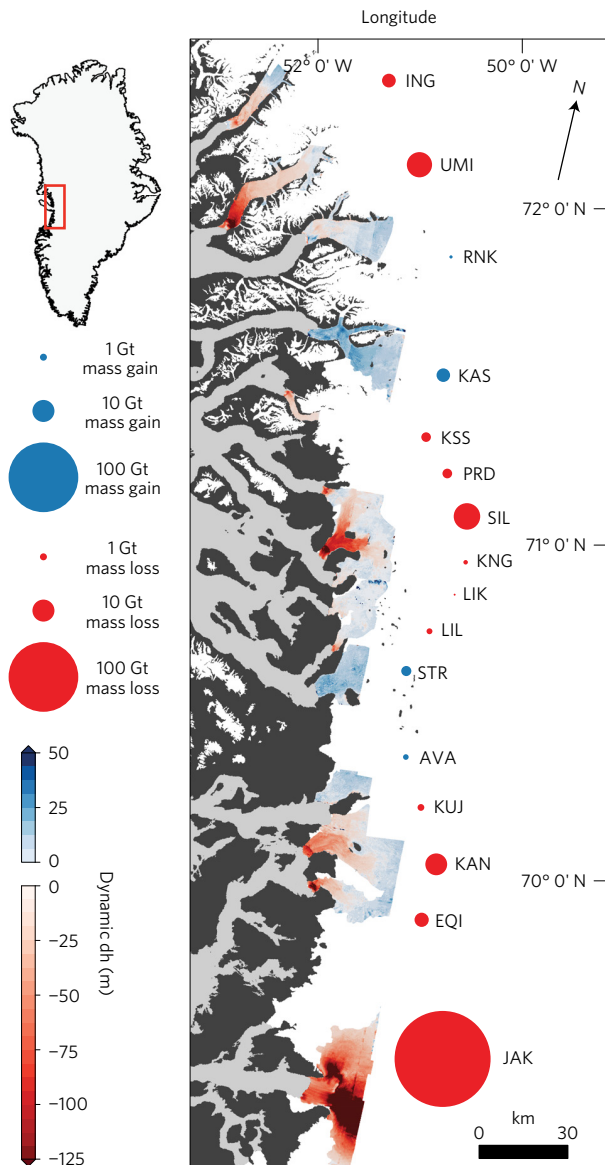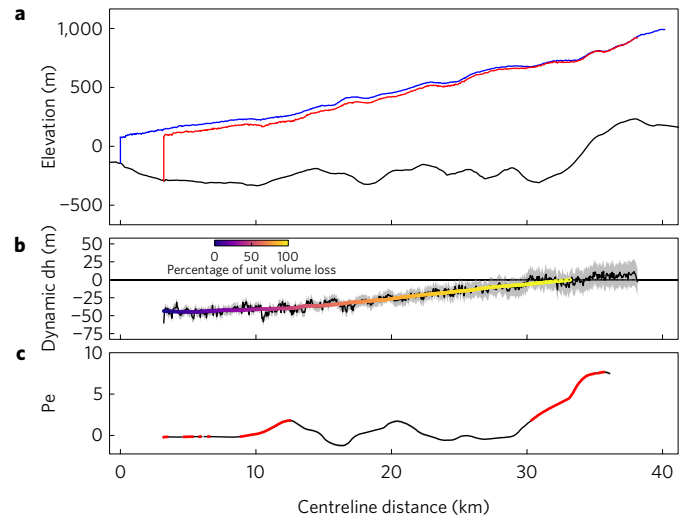
Figure 1 | Dynamic surface elevation change and mass loss. Surface elevation change from DEM differencing from 1985–present with surface mass balance (SMB) anomaly removed. Labels pertain to glacier names listed in Supplementary Table 2. Differences plotted on top of GIMP surface classification mask[25] with ice in white, ocean in light grey, and bedrock in dark grey. Circle areas are proportional to dynamic mass gain (blue) or loss (red).

KAN, Eqip Sermia (EQI) and JAK) while terminus positions of the thickening glaciers (KAS, STR and AVA) have remained stable (Supplementary Table 2). JAK alone accounts for more than 81% of the total mass loss in the study region; however, we are unable to quantify JAK's full mass loss due to the limited spatial extent of the available DEMs. UMI, SIL and KAN account for 84% of the remaining regional mass loss.

Kinematic wave theory

Our observations show that glacier thinning is greatest at glacier termini and decreases with distance up-glacier from the terminus until, where observable within the spatial extents of the DEMs, it reaches zero at some location along the centreline. This is consistent with the hypothesis that terminus retreat perturbs the force balance, causing thinning to propagate up-glacier[13,14]. The propagation of thinning along a glacier's length can be modelled as

Figure 2 | Centreline profile of Kangilernata Sermia (KAN). a, Elevations relative to the WGS-84 ellipsoid for 1985 (blue) and present-day (red) glacier surfaces and mass-conserving bed[20] (black) along the glacier centreline. **b**, Dynamic surface elevation change (black) with uncertainty from standard error propagation (grey, Methods). Moving average within window of 10 local ice thicknesses coloured by percentage of unit volume loss. **c**, Péclet number (Pe) calculated from the 1985 surface (black) with Pe running maximum (red). Shading reflects uncertainty (on the order of ±0.25 in this example) from standard error propagation (Methods).

a diffusive kinematic wave[21] (Methods). The competition between advection and diffusion of this wave, which reduce and enhance the up-glacier translation of the thinning perturbation, respectively, is given by the Péclet number (Pe, Methods). For relatively thick, flat ice, Pe is low and diffusion dominates, allowing a thinning perturbation to diffuse away from that location. Conversely, where ice is relatively thin and steep, such as over rises in basal topography, Pe is high because advection dominates and thinning perturbations will advect down-glacier. Thus, by computing Pe along a glacier centreline, we can empirically identify high Pe values at locations beyond which, up-glacier, diffusive propagation of terminus-initiated thinning will be limited.

To illustrate our approach, we compare Pe and observed elevation change of KAN along the glacier's centreline (Fig. 2). We perform a moving average on the thinning, within a window with a width ten times the local ice thickness, and calculate the cumulative averaged thinning from the terminus to each centreline location. We represent this as a percentage of total cumulative thinning observed along the entire length of each glacier's centreline, herein called '% unit volume loss' (coloured line in Fig. 2b). For KAN, we find that 100% of unit volume loss has occurred down-glacier of a rise in the bed at 35 km along the profile, where Pe reaches a maximum of 7.7 (Fig. 2c). At this location, down-glacier advection of thinning dominates, and terminus-initiated thinning cannot propagate up-glacier beyond this point. Downstream Pe values of less than 2 have allowed terminus-initiated thinning to diffuse up-glacier to this location.

Empirical threshold for inland thinning extent

We define 'Pe running maxima' as the locations along the centreline where Pe locally exceeds any downstream value of Pe (red on Fig. 2c). Pe running maxima are critical because once a thinning perturbation propagates beyond a local maximum in Pe and accesses lower Pe values, the thinning will continue to propagate up-glacier until it reaches yet higher Pe values. This effect is apparent for 11 West GrIS glaciers that have thinned at their termini (Fig. 3a); JAK is excluded because of incomplete DEM coverage. We find that 94% of the median unit volume loss (interquartile range of

93%–100%) occurs down-glacier of a Pe running maximum of 3. Pe running maxima of less than 3 can still be important by impeding the up-glacier propagation of thinning. This can be seen along the centreline of Lille Gletsjer (LIL), where a Pe running maximum of 1.8 near 4 km restricts 50% of the unit volume loss to this lowest reach, while more moderate thinning extends to 14 km, where Pe reaches 8.5 (Supplementary Fig. 11). Similarly, Pe running maxima of <3 and 2.2 are found close to the termini of KSS and PRD (Supplementary Figs 6 and 7), respectively, which buffer the thinning up-glacier of these locations from the stronger thinning near their termini.

The evaluation of Pe requires a relationship between glacier flow, ice thickness and surface slope. We test the robustness of our results by implementing four relationships and find that, in general, all formulations highlight the importance of the same geometric features (Supplementary Figs 2–16). An empirical Pe threshold can be identified for each formulation, beyond which dynamic thinning is limited (Supplementary Fig. 17). All ice flow formulations lead us to conclude that glacier geometry provides a dominant control on the inland extent of thinning.

Although glacier thinning changes glacier geometry, and therefore Pe, we note that even for UMI, second only to JAK in observed thinning at its terminus (>100 m), differences between the present-day Pe and the 1985 Pe are not significant (Supplementary Fig. 18). The locations of Pe = 3 vary significantly along glacier centrelines (from 6 km at Kangerluarsuup Sermia (KSS) to 243 km at JAK; Fig. 3b). The distance to these threshold crossings explains the spatial patterns of thinning within each catchment and provides an explanation for the observed heterogeneity in mass loss within the West GrIS region.

Our empirical threshold of Pe = 3 can be used to judge the relative susceptibility of glacier catchments to future terminus-initiated thinning. We expect 94% of mass loss to occur down-glacier of the Pe = 3 crossing, should terminus retreat occur, and for any glacier catchment, the further inland that this threshold is met, the greater the contribution to future sea-level rise will be. We expect similar variability in glacier geometry for catchments around the GrIS, which could lead to future heterogeneity in the dynamic response to terminus-initiated thinning. However, because the volume of inland thinning is correlated with the amount of terminus retreat, we note that our analysis cannot predict the expected mass loss for a particular glacier without an understanding of the future evolution of its terminus position. As an example, the Pe = 3 crossing for Sermilik (LIK) is second farthest inland in the study region; however, its terminus currently sits in relatively shallow water compared to the more deeply grounded glaciers (water depth at LIK shallows to 30 m just 500 m behind the present-day terminus). Thus, future terminus-driven perturbations at LIK are likely to be smaller than those at glaciers with more deeply grounded termini.

The Péclet number can be used to identify the glacier catchments where improved or long-term observations are needed most and provide provisional estimates of inland thinning extent, while numerical ice sheet models evolve to the point where catchment-scale heterogeneity can be resolved. Additionally, numerical models are only as good as the understanding that goes into building them, and certain processes and boundary conditions (for example, basal friction) may be inadequately represented. Our method circumvents the need for a deeper, but often poorly constrained, process-based understanding that is necessary for projection. The Péclet number is also useful for interpretation of thinning by identifying whether the dynamic response is due to terminus-initiated perturbations. Thinning down-glacier of the location where the Pe first crosses 3 may have originated at the terminus, whereas any significant thinning occurring up-glacier of that location is unlikely to have originated from the terminus. The thinning we observe within glacier catchments in West Greenland is currently dominated by a
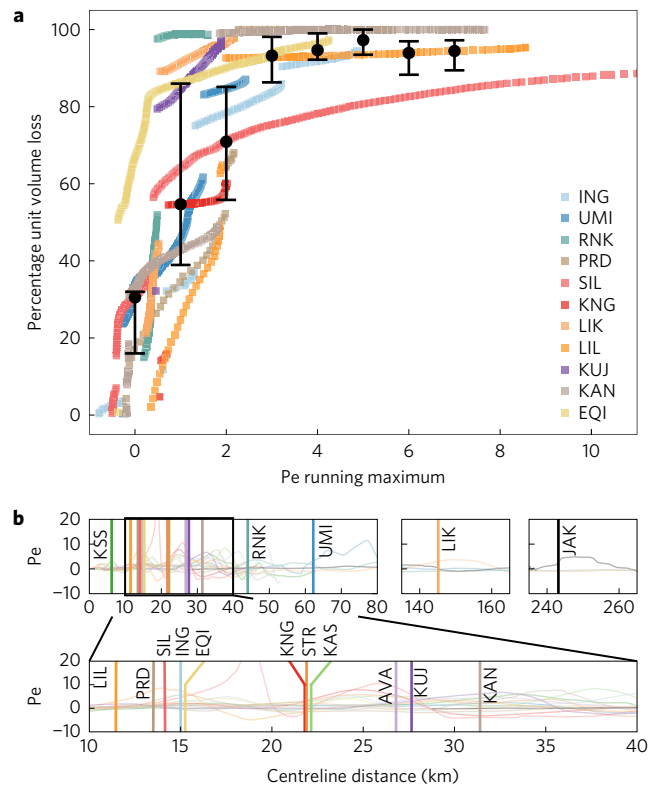
Figure 3 | Péclet number running maxima and percentage unit volume loss. a, Percentage unit volume loss plotted against the running maximum Pe for 11 dynamically thinning West Greenland outlet glaciers. Median percentage unit volume loss within bins of width 1 Pe are calculated for each glacier and black dots are medians of the glacier median values with error bars representing the 25th and 75th percentiles of percentage unit volume loss. **b**, Pe for 16 West Greenland outlet glaciers along their centrelines. Locations where the Pe first exceeds 3 are marked for each glacier.

response to terminus perturbations, which implicates some manner of ocean forcing. However, in the future, a different dynamic process may be responsible for glacier changes, and the Péclet number will help identify this.

Our study highlights significant spatial variability in the response of 16 West Greenland outlet glaciers to recent climatic forcing. This heterogeneity is explained by variations in local geometry (ice thickness, bed and surface topography) that influence the inland diffusion of thinning. Whereas previous authors have applied kinematic wave theory to understand the time-dependent evolution of glaciers[23,24], we demonstrate that the Péclet number explains spatially dependent dynamic changes. By applying the theory to a suite of glaciers, we define an empirical limit to upstream thinning, whether a glacier has retreated or not. Because the diffusion of terminus-initiated thinning is projected to be a large source of future contributions to sea-level rise for the GrIS (ref. 13), our approach enables identification of those glacier catchments most susceptible to future inland thinning and, thus, with the largest potential to increase sea level. Similarly, we can also use the Péclet number to identify those catchments with limited ability to dynamically respond. In West Greenland, RNK, UMI, JAK and LIK have the farthest inland Pe = 3 crossings. At JAK, we anticipate that ongoing dynamic thinning may eventually extend one third of the way across the entire GrIS at the latitude of JAK. The future response of LIK may be mitigated by the retreat of its terminus into shallow water. However, UMI and RNK have large potential to contribute further to future dynamic mass loss in the West Greenland region, and thus we recommend continued monitoring there.

Methods

Methods, including statements of data availability and any associated accession codes and references, are available in the online version of this paper.

References

1. Wouters, B., Chambers, D. & Schrama, E. J. O. GRACE observes small-scale mass loss in Greenland. *Geophys. Res. Lett.* **35,** L20501 (2008).
2. Harig, C. & Simons, F. J. Mapping Greenland's mass loss in space and time. *Proc. Natl Acad. Sci. USA* **109,** 19934–19937 (2012).
3. Schrama, E. J. O. & Wouters, B. Revisiting Greenland ice sheet mass loss observed by GRACE. *J. Geophys. Res.* **116,** B02407 (2011).
4. Velicogna, I., Sutterley, T. C. & van den Broeke, M. R. Regional acceleration in ice mass loss from Greenland and Antarctica using GRACE time-variable gravity data. *Geophys. Res. Lett.* **41,** 8130–8137 (2014).
5. Murray, T. *et al.* Extensive retreat of Greenland tidewater glaciers, 2000–2010. *Arct. Antarct. Alp. Res.* **47,** 427–447 (2015).
6. Csatho, B. M. *et al.* Laser altimetry reveals complex pattern of Greenland ice sheet dynamics. *Proc. Natl Acad. Sci. USA* **111,** 18478–18483 (2014).
7. Moon, T., Joughin, I., Smith, B. & Howat, I. 21st-century evolution of Greenland outlet glacier velocities. *Science* **336,** 576–578 (2012).
8. Kjaer, K. H. *et al.* Aerial photographs reveal late-20th-century dynamic ice loss in northwestern Greenland. *Science* **337,** 569–573 (2012).
9. Howat, I. M., Joughin, I., Fahnestock, M., Smith, B. E. & Scambos, T. A. Synchronous retreat and acceleration of southeast Greenland outlet glaciers 2000–06 ice dynamics and coupling to climate. *J. Glaciol.* **54,** 646–660 (2008).
10. Bevan, S. L., Luckman, A. J. & Murray, T. Glacier dynamics over the last quarter of a century at Helheim, Kangerdlugssuaq and 14 other major Greenland outlet glaciers. *Cryosphere* **6,** 923–937 (2012).
11. Khan, S. A. *et al.* Sustained mass loss of the northeast Greenland ice sheet triggered by regional warming. *Nat. Clim. Change* **4,** 292–299 (2014).
12. Enderlin, E. M. *et al.* An improved mass budget for the Greenland ice sheet. *Geophys. Res. Lett.* **41,** 866–872 (2014).
13. Price, S. F., Payne, A. J., Howat, I. M. & Smith, B. E. Committed sea-level rise for the next century from Greenland ice sheet dynamics during the past decade. *Proc. Natl Acad. Sci. USA* **108,** 8978–8983 (2011).
14. Nick, F. M., Vieli, A., Howat, I. M. & Joughin, I. Large-scale changes in Greenland outlet glacier dynamics triggered at the terminus. *Nat. Geosci.* **2,** 110–114 (2009).
15. Konrad, H. *et al.* Uneven onset and pace of ice-dynamical imbalance in the Amundsen Sea Embayment, West Antarctica. *Geophys. Res. Lett.* **44,** 910–918 (2017).
16. Pfeffer, W. T., Harper, J. T. & O'Neel, S. Kinematic constraints on glacier contributions to 21st-century sea-level rise. *Science* **321,** 1340–1343 (2008).
17. Nick, F. M. *et al.* Future sea-level rise from Greenland's main outlet glaciers in a warming climate. *Nature* **497,** 235–238 (2013).
18. Moore, J. C., Grinsted, A., Zwinger, T. & Jevrejeva, S. Semiempirical and process-based global sea level projections. *Rev. Geophys.* **51,** 484–522 (2013).
19. Korsgaard, N. J. *et al.* Digital elevation model and orthophotographs of Greenland based on aerial photographs from 1978–1987. *Sci. Data* **3,** 160032 (2016).
20. Morlighem, M., Rignot, E. & Willis, J. Improving bed topography mapping of Greenland glaciers using NASA's Oceans Melting Greenland (OMG) data. *Oceanography* **29,** 62–71 (2016).
21. Nye, J. F. The response of glaciers and ice-sheets to seasonal and climatic changes. *Proc. R. Soc. A* **256,** 559–584 (1960).
22. Pritchard, H. D., Arthern, R. J., Vaughan, D. G. & Edwards, L. A. Extensive dynamic thinning on the margins of the Greenland and Antarctic ice sheets. *Nature* **461,** 971–975 (2009).
23. Pfeffer, W. T. A simple mechanism for irreversible tidewater glacier retreat. *J. Geophys. Res.* **112,** F03S25 (2007).
24. van der Veen, C. J. Greenland ice sheet response to external forcing. *J. Geophys. Res.* **106,** 34047–34058 (2001).
25. Howat, I. M., Negrete, A. & Smith, B. E. The Greenland Ice Mapping Project (GIMP) land classification and surface elevation data sets. *Cryosphere* **8,** 1509–1518 (2014).

Author contributions

D.F., T.C.B. and G.A.C. designed the study. D.F. created the WorldView DEMs, calculated catchment mass changes, and performed the kinematic wave analysis. D.F., T.C.B. and G.A.C. interpreted the results. N.J.K. and K.H.K. created the 1985 DEM. M.M. processed the mass-conserving bed for the study region. B.N. and M.v.d.B. provided downscaled SMB data. All authors discussed the results and commented on the manuscript.

Additional information

Supplementary information is available in the online version of the paper. Reprints and permissions information is available online at www.nature.com/reprints. Publisher's note: Springer Nature remains neutral with regard to jurisdictional claims in published maps and institutional affiliations. Correspondence and requests for materials should be addressed to D.F.

Competing financial interests

The authors declare no competing financial interests.

Methods

1985 DEM and uncertainty. The 1985 DEM was created from aerial photos[19]. Total error in the 1985 DEM consists of two components: random error, herein called the 'noise floor' (ϵ_{noise}), and systematic error due to uncertainty in the positioning of the camera. Systematic error is quantified by the mean errors on the heights predicted by the photogrammetric model determined by the bundle block adjustment (ϵ_{bundle}). Spatial variability of the bundle block adjustment errors is governed by the location and geometry of the ground control; error will increase away from the margin, where ground control points are concentrated, into the interior of the ice sheet. The sum of the random noise and the systematic error components, in quadrature, yields the total error for the DEM (ϵ_{total}). Total DEM error can be found from differences in the DEM elevation and the elevation measured by airborne laser altimetry over a stable surface such as bedrock. Airborne laser altimetry is an appropriate control given that the uncertainty of the laser altimetry is an order of magnitude lower than the uncertainty in the DEM (ref. 8). Here, we use laser altimetry collected by NASA's Airborne Topographic Mapper (ATM).

To find the noise floor of the DEM, we first found total error (ϵ_{total}) in the 1985 DEM by comparing DEM elevations at elevation measurements from laser altimetry over stable bedrock surfaces with slopes less than 20° (ref. 19). This yielded a mean value for total error (ϵ_{total}) across the extent of the 1985 DEM of 4.1 metres. Next, we created a surface of bundle block adjustment errors, using linear interpolation based on Delaunay triangulation, and queried this error surface at the same bedrock locations as the total errors, yielding a mean value for bundle adjustment error (ϵ_{bundle}) of 2.3 m. The noise floor of the 1985 DEM was calculated as the difference between the squares of the two components:

$$\epsilon_{floor}^2 = \epsilon_{total}^2 - \epsilon_{bundle}^2 \qquad (1)$$

This yielded a value for the DEM noise floor (ϵ_{floor}) of 3.4 m and we assume the noise floor to be constant across the spatial extent of the DEM.

Finally, to obtain the total DEM error, we add the noise floor and spatially varying bundle block adjustment components, from the error surface, in quadrature:

$$\epsilon_{total}^2 = \epsilon_{noise}^2 + \epsilon_{bundle}^2 \qquad (2)$$

This provides us with a continuous surface representing the total error on the 1985 DEM and we query this at locations along all glacier centrelines to obtain uncertainties on the 1985 DEM elevations.

WorldView DEMs and uncertainty. We created 2012–2015 present-day DEMs from WorldView imagery using the NASA AMES Stereo Pipeline (ASP) software package[26]. Previous work has shown that WorldView DEMs over the Greenland ice sheet have a vertical uncertainty of 5.22 m and may contain a systematic vertical bias[26]. To remove the bias, vertical differences between each WorldView DEM and the 1985 DEM were found over bedrock, as defined by the GIMP surface mask[25], for slopes less than 20°, and the mean vertical offset was removed from each WorldView DEM.

Dynamic mass change and glacier catchments. Assuming the ice sheet was in balance from 1971 to 1988[27], we calculate the surface mass balance (SMB) anomaly as the departure from the 1971 to 1988 mean using RACMO2.3 model output, statistically downscaled to 1 km resolution[28], assuming a constant ice density of 917 kg m^{-3}, an appropriate assumption for the ablation zone of the glacier catchments where our analysis is focused. We plot the contour of where cumulative SMB is zero, and observe that our DEM differences lie entirely in the region where SMB is negative, indicative of the ablation zone (Supplementary Fig. 1). Modelled SMB from RACMO2.3 is precipitation (solid and liquid) minus surface sublimation, drifting snow erosion, and runoff. SMB anomaly is integrated temporally from 1985 to the year of each WorldView DEM used in the study. Dynamic surface elevation change was found by removing the elevation change due to SMB anomaly from the total elevation change calculated from DEM differencing.

Glacier catchments were delineated using standard watershed analysis by assuming that ice flows in the direction of the negative gradient of the ice surface. The GIMP DEM was used as the ice surface, providing a continuous surface over the entire ice sheet and allowing us to delineate the full catchment extents from the ice sheet margin to the ice divide.

Kinematic waves. To obtain the diffusive kinematic wave equation, the one-dimensional mass continuity equation is linearized about a datum state to obtain an advection–diffusion equation for ice thickness perturbations. The advection–diffusion equation for thickness perturbations can be expressed as:

$$\frac{\partial H_1}{\partial t} = \dot{b}_1 - \frac{\partial C_0}{\partial x} H_1 - \left(C_0 - \frac{\partial D_0}{\partial x} \right) \frac{\partial H_1}{\partial x} + D_0 \frac{\partial^2 H_1}{\partial x^2} \qquad (3)$$

where $\dot{b}_1$ is the SMB anomaly; the coefficients $C_0 = (\partial q / \partial H)_0$ and $D_0 = (\partial q / \partial \alpha)_0$; q is ice flux, H is ice thickness, α is the surface slope and x is the along-flow direction up-glacier from the terminus. The subscript '1' represents perturbation quantities and '0' represents the datum state. See Supplementary Information for a complete derivation of the kinematic wave equation.

By removing the thickness change due to SMB anomaly, $\dot{b}_1$, from the total observed surface elevation change, we investigate how glacier dynamics alone control glacier elevation changes. The second term, $(\partial C_0 / \partial x)H_1$, modulates the timing of local thickness change by introducing an over-damped component to the response which exponentially decays with time[21]. This response acts independently of nearby thickness perturbations. In contrast, the third and fourth (advective and diffusive) terms depend on the first and second spatial derivatives of the thickness perturbation, and thus depend on adjacent thickness changes. These two terms govern the along-flow propagation of H_1 and are the focus of our study. Previous studies have used a similar framework to study changes of tidewater glaciers in both Greenland and Alaska[23,24].

Thus, the spatial evolution of the thinning perturbation is governed by the advective and diffusive terms in equation (3) (third and fourth terms on the right-hand side). A thinning perturbation of some finite length will simultaneously advect and diffuse in both directions along-flow at rates governed by the glacier's geometry. We are interested in whether a thinning perturbation, extending from the terminus to an up-glacier location with length l, will advect down-glacier and be replenished by thicker ice from up-glacier or continue to diffuse up-glacier, beyond the location $x = l$. The relative rates of advection, or wave speed, and diffusion is given by the Péclet number (Pe), a non-dimensional ratio of the coefficient of advection, ($C_0 - \partial D_0 / \partial x$), to the coefficient of diffusion, D_0 (ref. 29):

$$Pe = \frac{(C_0 - \partial D_0 / \partial x)}{D_0} l \qquad (4)$$

where l is the length of the thinning perturbation (Methods). The values of C_0, D_0 and $\partial D_0 / \partial x$ are given by the dependence of local ice flux on surface slope, α_0, and ice thickness, H_0, respectively (equations (14)–(19) in Supplementary Information). For the rapidly flowing trunks of the outlet glaciers in our region of interest, we assume that ice flow is dominated by basal sliding and we use several commonly used relationships between ice flux, thickness and slope (commonly referred to as 'sliding laws') to evaluate the Péclet number (Methods).

The relationship described by the sliding laws (equations (12) and (13) in Supplementary Information) assume a balance between the driving stress and the basal shear stress, and ignores membrane stresses. Therefore, prior to calculating Pe, we perform a moving average of the bed and surface topography over a length of ten times the local ice thickness, a typical longitudinal coupling length for fast-flowing ice[30]. At each point along the centreline, α_0 and H_0 are calculated using the smoothed 1985 DEM and the smoothed mass-conserving bed[20], representing the pre-thinning geometry, and the length, l, is the distance from the terminus to the local point.

All sliding laws are valid only where surface slope is positive and we do not calculate the Péclet number where slope is less than or equal to zero. Basal water pressure in the effective pressure sliding law formulation is set to ice overburden pressure. The effective pressure law is invalid where the glacier approaches flotation, and we do not calculate the Péclet number where the difference between ice thickness and water pressure (in ice thickness equivalent) is less than or equal to 75 m.

Uncertainty. Uncertainties in the mass-conserving bed solution, the 1985 DEM and the WorldView DEMs are propagated through the moving averaging, through the analytic expressions for C_0, D_0 and $\partial D_0 / \partial x$ (equations (14)–(19) in Supplementary Information), through equation (4), and through the calculation for % unit volume loss. The procedure for creating the mass-conserving bed solution produces errors at each grid cell[20]. This yielded uncertainties in the Pe values, shown in grey shading on Fig. 2 and Supplementary Figs 2–16 in Supplementary Information.

Pe running maxima and unit volume loss. We define 'Pe running maxima' as the locations along the centreline where Pe locally exceeds any downstream value of Pe (red on Fig. 2c). Percentage unit volume loss is defined as the cumulative thinning from the terminus to each centreline location, as a percentage of total cumulative thinning observed along the entire length of each glacier's centreline (coloured curve on Fig. 2b). We binned values of percentage unit volume into windows of width Pe = 1 and calculated the median, 25th and 75th percentiles. We do not propagate uncertainties in percentage unit volume loss and running Pe maxima through these statistics calculations because uncertainties in the statistics are more sensitive to the scatter of values from all glaciers than the uncertainties in the individual values themselves.

Code availability. The code for the Péclet number calculation along glacier flowlines is available from the corresponding author upon request. The NASA AMES Stereo Pipeline, used to create DEMs from WorldView stereo imagery, is available for download at https://ti.arc.nasa.gov/tech/asr/intelligent-robotics/ngt/stereo.

Data availability. The 1985 DEM is available at http://dx.doi.org/10.7289/V56Q1V72. The mass-conserving bed is available at http://dx.doi.org/10.5067/AD7B0HQNSJ29. Present-day WorldView DEMs are available from the author upon request; however, some of the WorldView DEMs are also available through the ArcticDEM project at the Polar Geospatial Center at http://pgc.umn.edu/arcticdem. Downscaled 1 km RACMO2.3 surface mass balance data are available from B. Noël (b.p.y.noel@uu.nl) and M. van den Broeke (m.r.vandenbroeke@uu.nl) upon request.

References

26. Shean, D. E. *et al*. An automated open-source pipeline for mass production of digital elevation models (DEMs) from very-high-resolution commercial stereo satellite imagery. *Int. Soc. Photogramm.* **116,** 101–117 (2016).
27. Rignot, E., Box, J. E., Burgess, E. & Hanna, E. Mass balance of the Greenland ice sheet from 1958 to 2007. *Geophys. Res. Lett.* **35,** L20502 (2008).
28. Noël, B. *et al*. Evaluation of the updated regional climate model RACMO2.3: summer snowfall impact on the Greenland ice sheet. *Cryosphere* **9,** 1831–1844 (2015).
29. Cuffey, K. M. & Paterson, W. S. B. *The Physics of Glaciers* Chap. 11 (Academic, 2010).
30. Kamb, B. & Echelmeyer, K. A. Stress-gradient coupling in glacier flow: I. Longitudinal averaging of the influence of ice thickness and surface slope. *J. Glaciol.* **32,** 267–284 (1986).